Int. J. Electrochem. Sci., 8 **(2013)** 11877 - 11895

International Journal of
ELECTROCHEMICAL
SCIENCE
www.electrochemsci.org

Hot Corrosion Behavior of FeAl Intermetallic Compound Modified with Silver in Molten Salt Mixture

R. A. Rodríguez-Diaz[1, 2*], *J. Uruchurtu-chavarín*[2], *A. Molina-Ocampo*[2], *J. Porcayo-Calderon*[2], *M. E. Mendoza*[3], *S. Valdez*[4], *J. Juárez-Islas*[5].

[1] Facultad de Química-UNAM, Circuito Exterior S/N, Cd. Universitaria, C.P. 04510, México, D.F., MEXICO.
[2] U.A.E.M.-C.I.I.C.A.P. Av. Universidad 1001, Col. Chamilpa, 62500 - Cuernavaca, Mor., México
[3] Instituto de Física, Universidad Autónoma de Puebla, Apartado Postal J-48, Puebla 72570, México.
[4] Instituto de Ciencias Físicas-UNAM, Av. Universidad S/N, Col. Chamilpa, Cuernavaca, C.P. 62210, Morelos, México.
[5] Instituto de Investigaciones en Materiales-UNAM, circuito exterior S/N, Ciudad Universitaria, C. P. 04510, México DF, México.
[*]E-mail: rdiaz.unam@gmail.com

Received: 30 May 2013 / *Accepted:* 27 August 2013 / *Published:* 10 September 2013

The hot corrosion behavior of Fe40Al intermetallic alloyed with 2.5 at. % Ag in KCl-$ZnCl_2$ (1:1M) at 450 °C has been studied and assessed by means of electrochemical techniques. Techniques included potentiodynamic polarization curves, linear polarization resistance (LPR) and electrochemical impedance spectroscopy (EIS) measurements. Furthermore thermodynamic stability phase diagrams were calculated and elaborated in order to improve the understanding of the corrosion mechanism. Results have shown that addition of Ag increase the corrosion rate. Besides, corrosion potential of Fe-Al-Ag alloy resulted nobler. Ternary Fe-Al-Ag alloy exhibited a more noble corrosion potential but a bigger corrosion rate than the 304 SS specimen corroded under the same experimental conditions. Corrosion behavior is explained in terms of the stability of the corrosion products formed film.

Keywords: FeAl aluminide, intermetallic compound, hot corrosion, electrochemical technique.

1. INTRODUCTION

Nowadays, accelerated urbanization and diversification of industrial sectors have led to the production of enormous quantities of wastes; a considerable portion of which is made up of organic matter. These wastes have been considered as detrimental to public health, ecosystem and the environment, if not correctly managed. The economic and financial impacts of these wastes cannot be ignored and their management has become a principal environmental concern. Incineration is a potent technique for organic combustible waste treatment and disposal, mainly because of the substantial

volume reduction, energy recovery, and the destruction of disease-causing microorganism and other toxic organic compounds [1].

Waste incinerators both produce and consume energy. In a large majority of cases, the energetic value of the waste exceeds the process demands and this result in the net export of energy. There are three ways of recovering energy: all-electric, all-thermal and combined heat and power [2].

Alloys used for applications involving high-temperature processes, such as combustion and high-power operations, sometimes undergo an aggressive mode of corrosion attack linked with formation of salt deposits on their surfaces at elevated temperatures [3]. It has been reported that 5–10% of operating costs in such plants are associated to corrosion failure at high temperature and related maintenance costs [4, 5].

Numerous variables, including alloy composition and amount of deposit salt, gas composition, temperature, temperature cycling, erosion, alloy composition, and alloy microstructure, have direct effects on severity of hot corrosion [6].

Severity of corrosive environments at metal/molten salt interface is influenced by penetration depth of corrosive species through scales. Protective oxide films, derived from alloying elements, play an important role in preventing corrosion attack [7]. As a result of this corrosion phenomenon, a porous and poorly adherent oxide scale is formed on surface of attacked alloy, which does not have an acceptable capability to protect the alloy in harsh, corrosive conditions [8].

One possible strategy to enhance energy conversion efficiency by mitigating superheater corrosion is via alloy modification. While accelerated corrosion is repeatedly observed for common, iron-based, superheater alloys with 1–2% Cr, higher alloyed steels such as austenitic stainless steels or nickel-base alloys have shown greater corrosion resistance [9,7] and are candidate materials for tubes and/or coatings.

FeAl base intermetallic alloys are of great interest in the industry for structural and high temperature applications mainly because of their low density and the low cost of the materials used for their production [10]. Besides, Al concentration of these alloys induces the formation of a passive aluminum oxide scale which is responsible of their high resistance to oxidation [11], sulphidation [12] at high temperatures and hot corrosion in molten salts [13, 14].

In order to obtain more information about the mechanisms of corrosion that occurs in alloys exposed to the aggressive environment involved in high-temperature and/or combustion processes, electrochemical techniques are more appropriate than conventional gravimetric methods in which the weight loss is measured.

Mohammadi and Alfantazi [15] studied the corrosion behavior of Inconel 625 alloy exposed to molten salt consisting of 47$PbSO_4$–23 ZnO–13 Pb_3O_4–10Fe_2O_3–7$PbCl_2$ (wt.%) under air atmosphere at 600, 700 and 800 °C, utilizing potentiodynamic polarization, EIS and weight-loss measurement techniques. The authors observed a general surface corrosion, intergranular corrosion, formation of voids and a network of distributed pores on surface and cross-section, plus internal oxidation and sulfidation. Besides, in this study, the EIS data fitted to a porous and non-protective barrier layer electrochemical model.

Otero et al. [16] studied the corrosion behavior of a 12CrMoV alloy in contact with a molten mixture of (52-48) mol.% $PbCl_2$-KCl, similar to that found in waste incineration plants. In this

investigation, the corrosion kinetics was analyzed using continuous-current electrochemical techniques and electrochemical impedance spectroscopy (EIS). According to EIS experiments, the authors discovered in all cases tested, a diffusion-control mechanism. The R_p obtained from these experiments are in a good agreement with the R_p obtained by (direct current) dc experiments.

Zeng and Li [17] studied the hot corrosion behavior of the Ni-based superalloy M38G covered with a film of molten $0.9Na_2SO_4–0.1K_2SO_4$ (mole fraction) by EIS at 900 °C in air. For comparison, the corrosion of the alloy immersed in molten $(Na,K)_2SO_4$ was also examined. The authors discovered that contrary to the corrosion in deep molten salt, the corrosion of the alloy in the presence of a film of fused salt presented the characteristics of two capacitive loops for all the duration of the experimental test. Equivalent circuits representing the corrosion of the alloy in both corrosion conditions are proposed to fit the impedance spectra and electrochemical parameters in the equivalent circuits were also calculated.

This work deals with an electrochemical study of the effect of adding 2.5 at.% Ag to a Fe40Al intermetallic alloy exposed to a salt mixture composed of KCl-$ZnCl_2$ (1:1M) at 450 °C on its corrosion behavior. The aim of present investigation is to find out a potential improvement for incinerator heat exchanger linings that will better tolerate the extreme conditions of heat and abrasion experienced by these components.

2. EXPERIMENTAL PROCEDURE

2.1 Materials

Cast ingots of binary Fe-40Al (at. %) and ternary Fe40Al2.5Ag (at. %) alloys were elaborated using a high-frequency induction furnace at approximately 1500°C in air. High purity (99.9 %) Fe, Al and Ag were placed in a silicon carbide crucible for induction melting. The molten Fe-40Al and Fe40Al2.5Ag alloys were poured into a rectangular copper mold and subsequently solidified during cooling until room temperature was reached, obtaining in this way a coarse grain microstructure.

2.2 Sample preparation

The produced ingots were cut by a diamond wheel cutter into small rectangular parallelepiped pieces of surface area ranging from 1.5 to 2.5cm^2. The electrical contact was made by welding a Ni20Cr wire to the specimen. Once welded to the specimen, the wire was put inside an alumina tube (2 mm inner diameter), so that the specimen remained at one end of the tube, where it was sealed with a refractory cement. The experimental apparatus used in the present study is very similar to that employed in a previous research [18].

2.3 Electrochemical techniques

Electrochemical techniques for characterizing the corrosion at high temperature included linear polarization (LPR), potentiodynamic polarization curves and electrochemical impedance (EIS) measurements. The body of the test cell was a 25 ml alumina crucible.

The most important elements were a reference and auxiliary electrodes, made of a 0.5 mm diameter (Pt) wire inside a mullite tube and filled with ceramic cement. The amount of salt in each run was 0.5 g for an exposed area of 1.0 cm^2 under static conditions, without stirring the molten salt. The electrical contact was made by welding an 80 wt. % Cr–20 Ni wire to the specimen.

Polarization curves were obtained by polarizing the specimens from -500 to +1000 mVPt with respect to the free corrosion potential value, E_{corr}, at a scanning rate of 1.0 mV/s. Corrosion current density values, I_{corr}, were calculated by using the Tafel extrapolation method taking an extrapolation zone of ± 250 mV around the E_{corr} value.

LPR measurements were carried out by polarizing the specimen from –10 to +10 mV with respect to E_{corr}, at a scanning rate of 1 mV/s, repeated every 20 minutes over a period of 24 hours. EIS measurements were done in the frequency interval of 0.05 to 30000 Hz at the E_{corr} value by using a PC4-300 Gamry potentiostat. The amplitude of the input sine-wave voltage was 10 mV.

Three measurements were performed in each case. The working salt consisted of 500 mg/cm^2 of an eutectic mixture of KCl-$ZnCl_2$ (1:1 M analytical grade) for each test. The testing temperature was 450ºC in static air condition. Prior to the tests, the specimens surfaces were prepared by the standard technique of grinding with SiC from 180 to 1200 grit emery paper and polished with 1 μm alumina slurry, after, the sample was washed with distilled water in an ultrasound apparatus.

2.4 Microstructural analysis of as-cast and corroded specimens.

Both as-cast and corroded specimens (taken after the LPR measurements) were mounted in bakelite. Metallographic preparation of encapsulated specimens was performed by grinding the specimens from 180 to 2000 grit paper and polished with 1 μm alumina slurry.

In order to determine crystal structure and phases identification in as-cast specimens, a Siemens 5000 X-ray diffractometer was employed, using Cu tube (K_α line radiation: λ = 0.15406 nm), and a diffracting beam graphite monochromator. The XRD patterns were recorded in the 2θ range from 20 to 80° (with step size 0.02, time per step 0.6 s).

The as-cast and corroded specimen surfaces were analyzed with a scanning electron microscope (SEM) with an accelerating voltage of 25 keV. Chemical microanalysis was carried out with an energy dispersive X-ray analyzer (EDX) attached to the SEM.

3. RESULTS AND DISCUSSION.

3.1 Microstructural characterization of un-corroded alloys.

3.1.1 Microstructure characterization by scanning electron microscopy.

The microstructure of the as-cast Fe40Al alloy is shown in Figure 1 a), exhibiting grains with a predominantly columnar morphology. XRD, SEM and chemical analyses using the EDS technique did not reveal the presence of precipitates on the surface of this alloy. This observation is consistent with the wide interval of composition (35-50 at. % Al) which contains a FeAl phase with a B2-type crystal structure according to the phase diagram for the Fe-Al system [19]. This alloy presented a chill-type

microstructure with three typical grain morphologies: chill, equiaxed and columnar. The mean size of chill morphology grains was 276 ± 88 μm, the dimensions of the columnar grains were 280 ± 94 μm in width and 2200 ± 130 μm in length and the size of equiaxed morphology grains was 548 ± 91 μm. Figure 1 b) displays the microstructure of ternary Fe40Al2.5Ag alloy at a higher magnification. This illustration show light gray precipitates with round borders uniformly distributed inside a grain of FeAl matrix alloy. According to XRD and point chemical analyses, these light gray precipitates correspond to pure Ag phase.

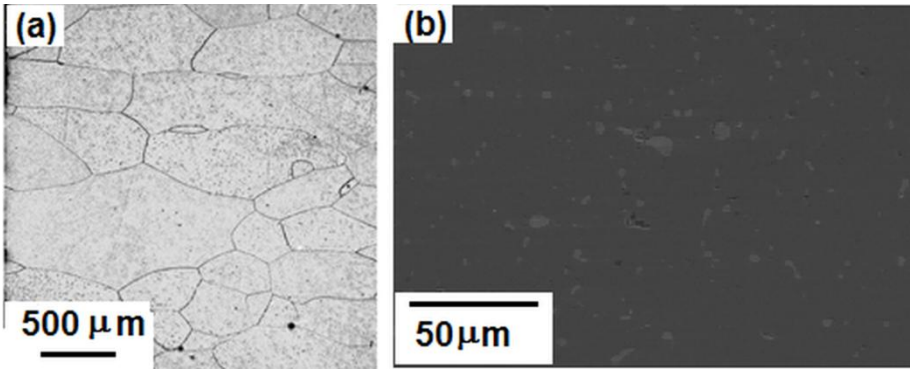

Figure 1. Microstructures of the as-cast alloys a) Fe40Al and b) Fe40Al2.5Ag.

3.1.2. Microstructural characterization of un-corroded alloys by X-Ray Diffraction (XRD) technique.

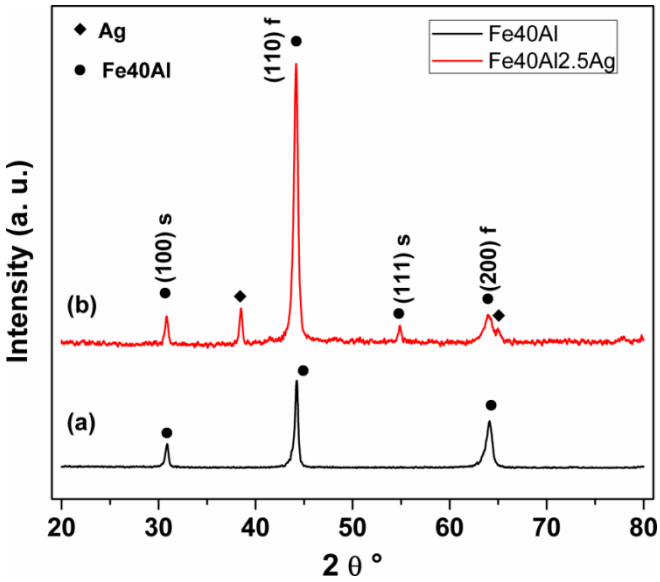

Figure 2. X-Ray diffraction patterns of the as-cast alloys a) Fe40Al and b) Fe40Al2.5Ag.

Figure 2 shows the XRD profiles of as-cast Fe40Al and Fe40Al2.5Ag (at. %) alloys. XRD patterns belonging to binary Fe40Al alloy exhibits only, the fundamental (f) and super lattice peaks (s) corresponding to a cubic B2 (CsCl) type ordered crystal structure [20, 21] as shown in Figure 2 a).

While the Fe40Al2.5Ag alloy displays the presence of peaks belonging both to the FeAl phase with a B2 ordered crystalline structure and the Ag phase with Fcc-type crystal structure, as shown in Figure 1 b). This finding indicates that all the Ag content did not entered in solid solution in FeAl matrix; but rather, this element precipitated uniformly distributed in this binary alloy. This behavior is due to the immiscibility of Ag in both Fe and Al elements according to Fe-Ag and Fe-Al binary alloy phase diagrams [22, 23].

Additional peaks pertaining to second phases or precipitates were not detected in Figure 1 a), suggesting that a single monolithic FeAl binary alloy is formed without the presence of precipitates. Figures 2 a), b) and c) do not exhibit all diffraction peaks, which is related to a large grain size and a preferred surface crystallographic orientation on samples.

3.2. Potentiodynamic polarization curves.

Polarization curves for binary Fe40Al and ternary Fe40Al2.5Ag alloys are shown in Figure 3. The polarization curves for Fe40Al2.5Ag alloy present a passive region with the possible formation of two different passive oxide compounds at about 0 volts and 175 volts, respectively. Fe40Al intermetallic alloy displays an active behavior only, with an E_{corr} value close to −331 mV and a corrosion rate, expressed in terms of the I_{corr} value near to 0.35 mA/cm^2. For the Fe40Al alloy a depolarizing region with fast dissolution in the anodic branch could be observed with the possible formation of non-protective corrosion products, reaching a limit current region at high anodic over-potentials at about 200mV. With the addition of Ag, the E_{corr} shifted towards positive side values of the vertical axis, reaching a value of −98 mV. In the same manner, the corrosion current density value increased with the addition of 2.5Ag. Thus, the addition of Ag increases the corrosion current density value, which means that this element induces a deleterious effect in the corrosion behavior of Fe40Al alloy. A similar behavior was reported in a previous research. Salinas et al. [24] studied the effect of adding silver to Fe40Al alloy on its corrosion behavior when the alloy was exposed to NaCl-KCl molten salt mixture at 670 °C. The authors reported that addition of Ag turned the E_{corr} value more noble and the I_{corr} value was increased.

Porcayo et al., [25] reported a value of the corrosion potential E_{corr} equal to -141 mV with an I_{corr} value of 1.89 mA/cm^2 in a 304 SS sample that was corroded in the same salt mixture (KCl-$ZnCl_2$) at 450 °C. Therefore, binary Fe40Al alloy studied in present work exhibit a more active corrosion potential but a lower corrosion rate than 304 SS under these test conditions. By the other side, ternary FeAlAg alloy exhibited a more noble corrosion potential but a bigger corrosion rate than the 304 SS sample corroded under the same experimental conditions.

Porcayo et al., [25] reported a current density value I_{corr} of 3.6 mA/cm^2 in a Ni20Cr wt % coating deposited on 304 stainless steel that was corroded in the same salt mixture (KCl-$ZnCl_2$) at 450 °C. Therefore, binary FeAl alloy presented a lower corrosion rate (expressed in terms of I_{corr}) than Ni20Cr wt% coating deposited on 304 SS corroded under the same conditions. However, after Ag addition the I_{corr} value shifted to 9 Ohm.cm^2. Thus, Fe40Al2.5Ag alloy presented a bigger corrosion rate than Ni20Cr wt% coating.

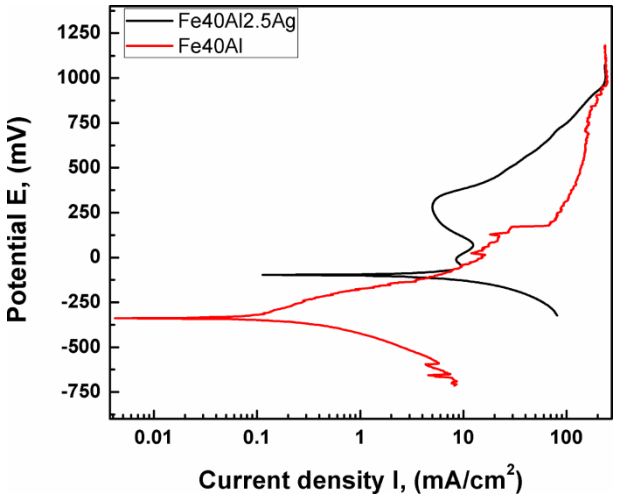

Figure 3. Polarization curves for Fe40Al alloyed with 2.5% Cr, Ti, and Ag in the KCl + $ZnCl_2$ mixture at 670°C.

3.3 LPR measurements.

The R_p values as a function of immersion time for Fe40Al binary alloy display variability but with a trend to increase as a function of time suggesting a decrease in its corrosion rate see Figure 4. On the other hand the Fe40Al2.5Ag´ R_p values are lower than the former ones, and exhibit a steady state condition with a slight increasing trend along the time of immersion, with average values around 80 ohms cm^2, but below the R_p´ values displayed by the FeAl alloy. This behavior is in accordance with the polarization curves shown in Figure 3, and can be due to the passive layer formed over the surface of the Fe40Al2.5Ag alloy.

In a previous investigation, Rodriguez et al. [26] measured the change in the R_p value with time for binary Fe40Al and ternary Fe40Al2.5Cr or Fe40Al2.5Ti alloys in the KCl+$ZnCl_2$ mixture at 450°C. The authors reported that both additions of Cr and Ti to Fe40Al alloy induced an increment of R_p values under the same experimental conditions of the tests. In contrast, addition of silver to Fe40Al promoted a decrement of the mean R_p value over the whole exposure time.

The ternary Fe40Al2.5Ag alloy exhibited mean values of R_p near to 100 Ohm.cm^2, while the mean R_p values of Fe40Al alloy resulted near to 300 Ohm.cm^2, see Figures 5 a) and b). This behavior is associated to the higher corrosion rate of FeAlAg alloy as compared with binary alloy. A previous research, reported a similar effect after the addition of Ag to a Fe-Al intermetallic alloy. Salinas et al. [24] studied the effect of adding Li, Ni, Ag and Cu to Fe40Al alloy on its hot corrosion behavior when the alloy was exposed to NaCl-KCl molten salt mixture at 670 °C. The authors reported that addition of Ag, Ni and Cu increased the corrosion rate measured in terms of the I_{corr}.

Figure 5 a) and b) display the change in the R_p and Potential values with time for (a) Fe40Al alloy and (b) Fe40Al2.5Ag alloy exposed to the KCl+$ZnCl_2$ mixture at 450°C. In these illustrations is clearly observed that the corrosion potential and the R_p values present an inverse correlation. The corrosion potential becomes active due to the corrosion process, while the R_p increased due to the film formation process. The film responsible for the increment of R_p values, is composed mainly by a

mixture of iron and aluminum oxides, see chemical analyses of elements in Figures 8 b), c) and d) and also in Figures 9 b), e) and h). At 20 hours a transient value for the corrosion potential was observed returning to previous corrosion potential values. This event could be ascribed probably to a galvanic local event over the surface with a repassivation-breakdown process.

The ternary Fe40Al2.5Ag alloy presents more active corrosion potentials, reaching the steady state values after 5 hours of immersion, at about -1175 volts. As seen before in Figure 4, the R_p values remained fairly constant, suggesting an almost constant dissolution as a function of time.

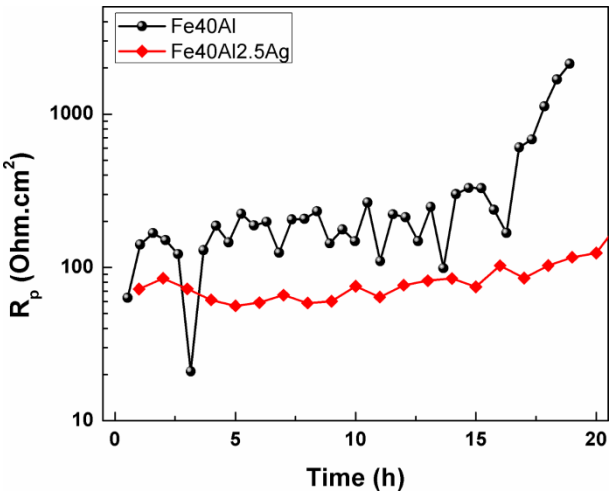

Figure 4. Change in the R_p value with time for binary Fe40Al and ternary Fe40Al2.5Ag alloys in the $KCl+ZnCl_2$ mixture at 450°C.

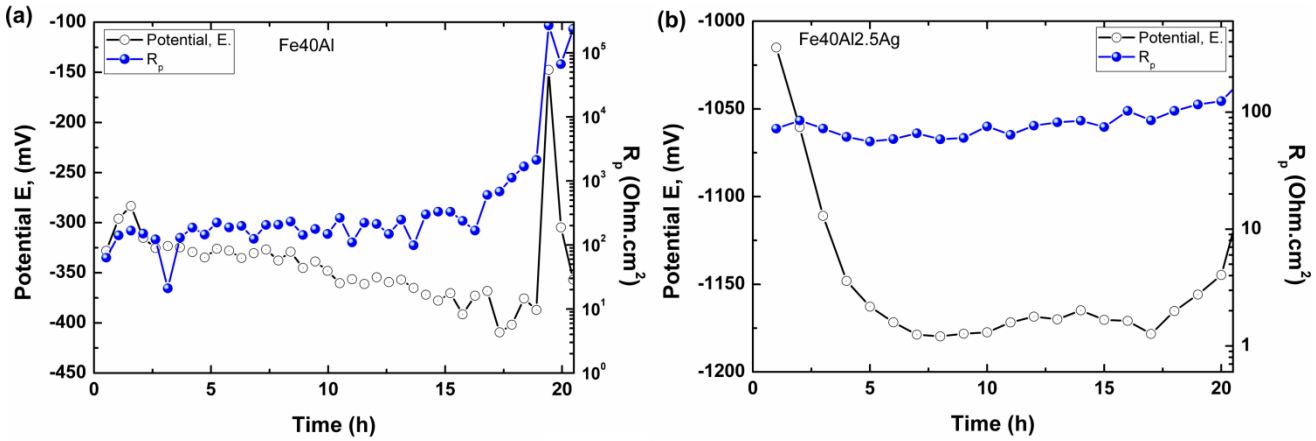

Figure 5. Change in the R_p and Potential values with time for (a) binary Fe40Al alloy and (b) ternary Fe40Al2.5Ag alloy, in the $KCl+ZnCl_2$ mixture at 450°C.

3.4. EIS measurements.

Nyquist diagrams for unalloyed Fe40Al intermetallic exposed to the $KCl+ZnCl_2$ mixture at 450 °C are displayed in Figure 6 a). For immersion times of 0 and 5 hours, the plots describe a single capacitive-like semicircle, and its diameter increasing with time. This diagram indicates that the

corrosion process is under charge transfer from the metal to the electrolyte through the double electrochemical layer [27]. For times greater than 5 hours, in addition to the high-frequency capacitive semicircle there is an uncompleted low-frequency semicircle. The diameter of the low-frequency semicircle is much bigger than that for the high-frequency semicircle and it has a trend to decrease as time elapses. The appearance of a large capacitive loop at the low-frequency region may denote the formation of a protective scale on the alloy surface which is in accordance with polarization curve of Fe40Al alloy shown in Figure 3. This behavior can be due to the formation of a layer of corrosion products composed mainly by a mixture of Al and Fe protective oxides and other compounds such as metals chlorides, see the chemical mappings displayed in Figure 8 b), c), d), e) and f). The presence of aluminum and iron oxides can be confirmed by looking at the thermodynamic stability phase diagram Fe-Al-Ag-Cl-O displayed in Figure 11, where Al and Fe oxide are stable across a wide interval of oxygen partial pressure (P_{O2}).

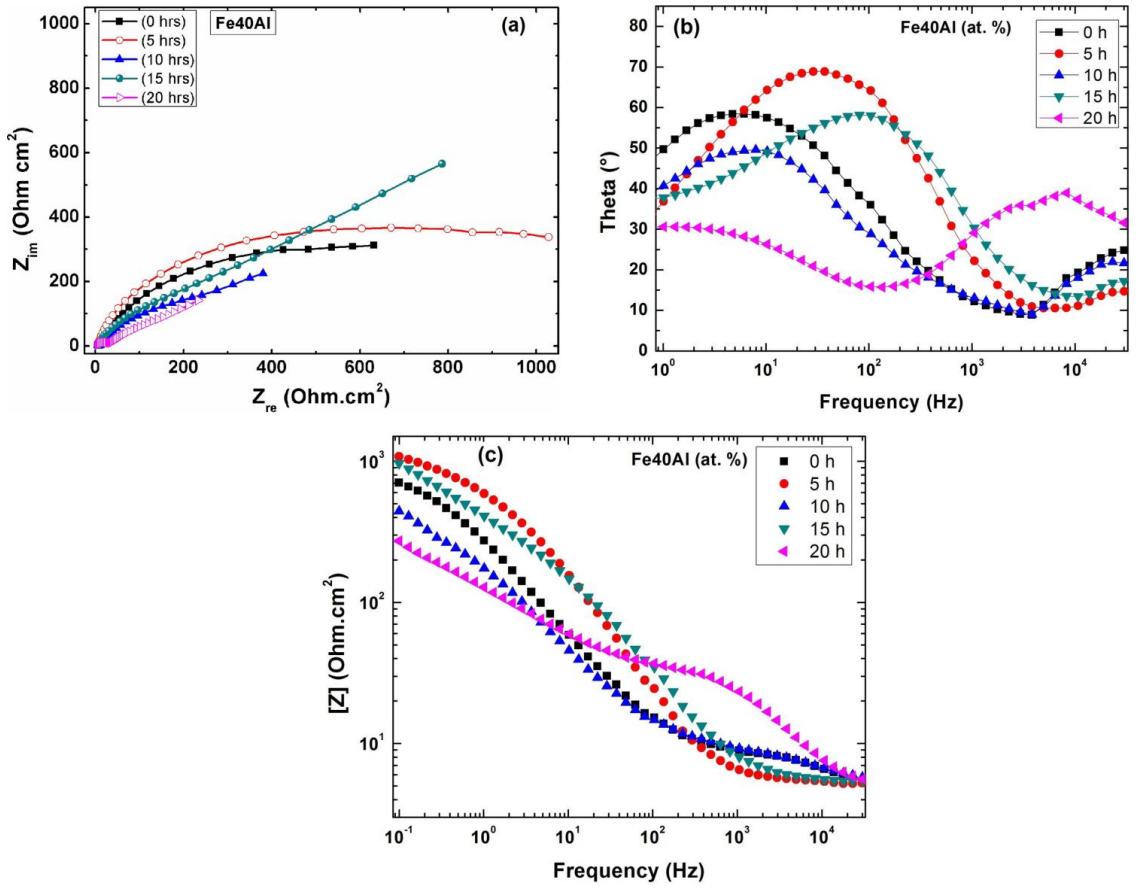

Figure 6. (a) Nyquist, (b) Bode and (c) Bode phase diagrams for Fe40Al corroded in the KCl+$ZnCl_2$ mixture at 450°C.

The bode impedance diagram shows two slopes and flat regions at high and low frequencies corresponding to the solution resistance at high frequency and the charge transfer resistance at low frequency, see Figure 6 c). The slope corresponds to the double layer capacitance and relates to a one time constant RC.

The Bode phase shift diagram, Figure 6(b), shows a single peak around 100 Hz, indicating the absence of a protective layer before applying the stress, and related to the double layer capacitance. However, as soon as the stress was applied, the presence of two overlapped peaks appeared, indicating the presence of a protective corrosion products layer, therefore suggesting that the crack walls may be covered by corrosion products. The aggressive ions have to diffuse through this layer and give rise to the diffusion process shown by Nyquist data.

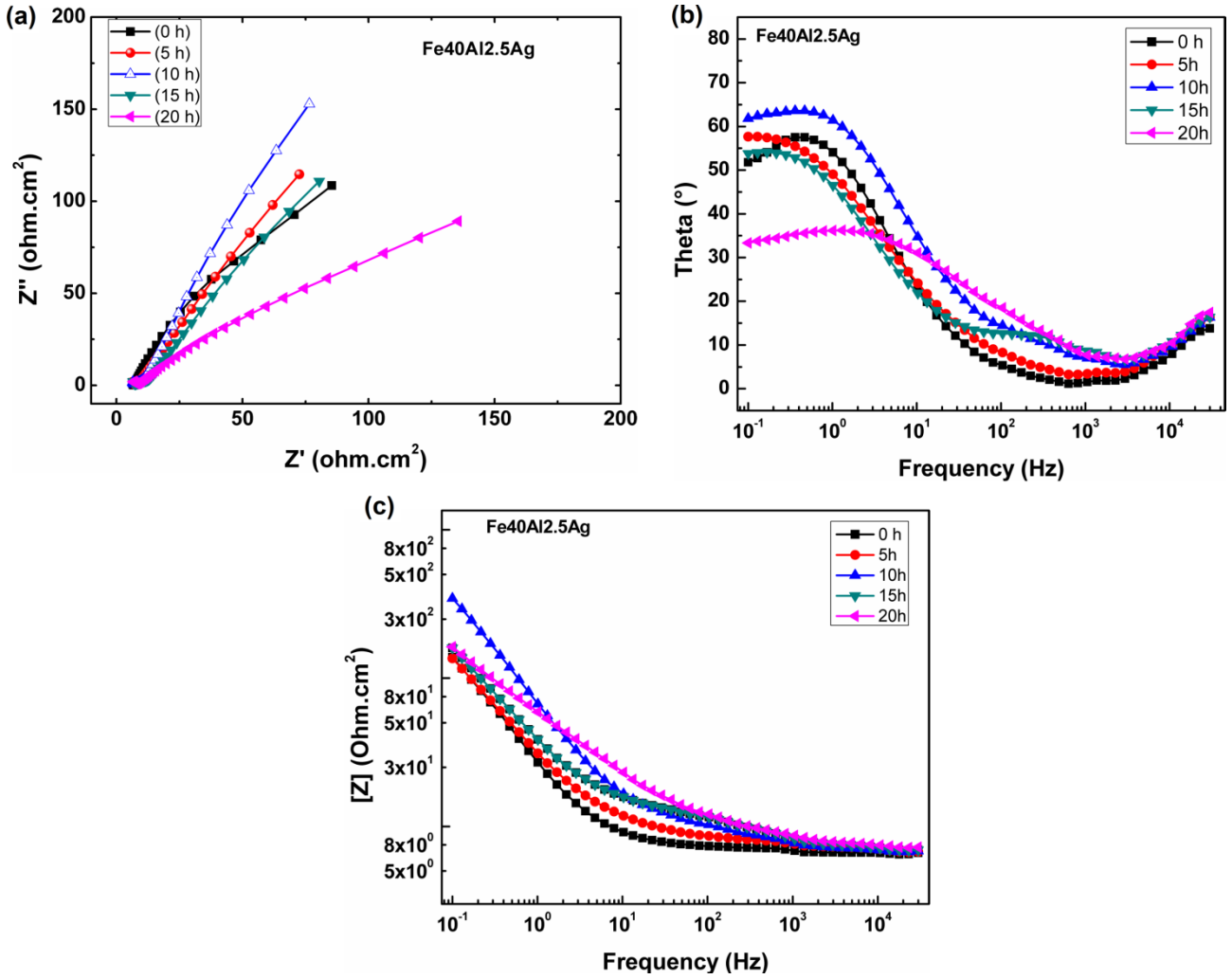

Figure 7. (a) Nyquist, (b) Bode and (c) Bode phase diagrams for Fe40Al2.5Ag alloy corroded in the KCl+$ZnCl_2$ mixture at 450°C.

Nyquist diagrams for ternary Fe40Al2.5Ag intermetallic alloy exposed to the KCl+$ZnCl_2$ mixture at 450 °C are presented in Figure 7 a). A high frequency capacitive semicircle associated to the charge transfer accompanied with a straight line diffusion process, starting to fold down at higher times of immersion associated to a limited diffusion layer and adsorption process, are clearly seen. The Bode impedance diagram (Figure 7c) shows a high frequency low impedance flat regions corresponding to the solution and charge transfer resistance and a low frequency slope associated to mass transport impedance (see Figure 7 b)).

The phase shift diagrams shown in Figure 7 b), shows at least two peaks at high and low frequencies related to the double layer and mass transport capacitance. Two overlapped peaks appeared at higher frequencies after five hours of immersion, indicating the presence of a corrosion products layer. The impedance behavior observed can be ascribed to the active conditions promoted by the Ag precipitates that will induce galvanic corrosion effects due to its noble potential with respect to the Fe-Al alloy components, promoting localized attack. Total impedance values remained almost the same ($2x10^2$ ohm.cm^2) except for the ten hour immersion measurement, where a total impedance slight increase was observed. All these is in accordance with the corrosion potential behavior and polarization resistance values as a function of time, observed and presented in Figures 4 and 5.

3.5. Microstructural characterization of corroded alloys.

After the LPR tests, some areas of corroded alloys were analyzed by means of scanning electron microscopy technique (SEM). Corrosion morphology of Fe40Al binary alloy together with the corresponding X-ray mappings of Al, Fe, O, Cl and Zn is shown in Figure 8.

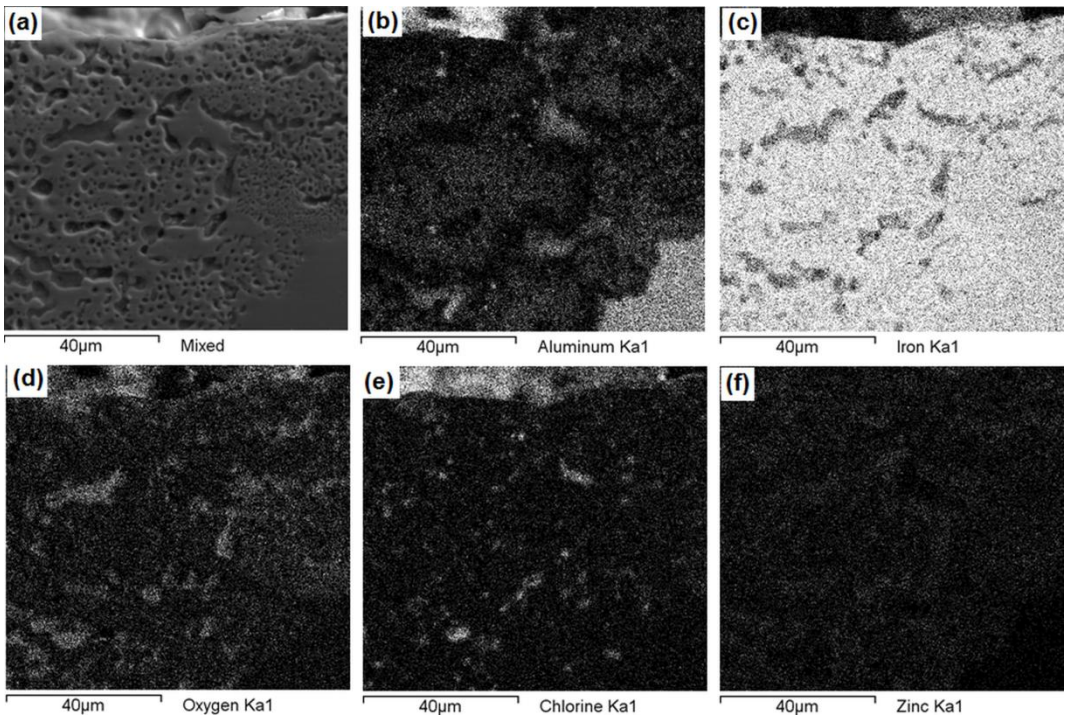

Figure 8. Photomicrographs of (a) Fe40Al corroded in the KCl+$ZnCl_2$ mixture at 450°C together with X-ray mappings of (b) Al, (c) Fe, (d) O, (e) Cl and (f) Zn.

Figures 8 b) and d), denote the existence of Al and O on the external layer, in these illustrations can be observed a discontinuous character of the Al layer, these findings led us to infer that there was some Al_2O_3 layer formed on top surface of the alloy. The presence of protective aluminum oxide film is justified by observing the thermodynamic stability phase diagram that displays a wide region in

which the aluminum oxide is stable, see Figure 11. Besides, previous investigations have reported aluminum oxide scale formation on iron aluminides's surface [28, 29]. In addition to this, Figure 10 e) denotes the presence of Cl beneath the Al_2O_3 superficial layer, which indicates that the molten salt had dissolved the oxide scale and permeated through it. This rapidly degraded the oxide´s protective properties, leading to a continuous degradation of the ternary alloy. According to $ZnCl_2$-KCl phase stability diagram [30], the $ZnCl_2$–KCl salt mixture was melted at experimental operation temperature, making the creation of protective layers over these Fe-Al alloys more difficult.

Aluminum depletion shown in Figure 8 b) is caused by a displacement reaction in the initial stages of the corrosion process in accordance with reaction 2 included in Table 2. As a direct consequence, an iron-enriched subsurface zone below the protective aluminum oxide located at surface of FeAl based alloy is formed in the ternary alloy matrix, see Figure 8 c). Iron produced in this way, is easily attacked by the chloride melt. Furthermore, free chlorine ions liberated by reaction 3 included in table 2, may penetrate easily inwards as a dissolved or gaseous species, trough pores of corrosion products and oxide scales, and concentrate near the alloy/scale interface. Demetallification of Al under scale alloy interface induces an increment of iron activity; besides, in this local region the chlorine partial pressure is high, so iron reacts with chlorine to form $FeCl_2$ according to reaction 10 included in Table 2. Formation of $FeCl_2$ produces significant scale disintegration due to the large growth of stresses derived from the large volume expansion created when the bold centered cubic crystal structure of Fe transforms to a monoclinic crystal structure corresponding to the $FeCl_2$ phase. Scale disruption leads to a deeper penetration of oxygen as evidenced in Figure 8 d). Once $FeCl_2$ was formed, after reacted with oxygen to form iron oxide according to reaction 9 included in Table 2. This induced the formation of a microporous surface film on the ternary alloy, allowing additional penetration by oxidants [31].

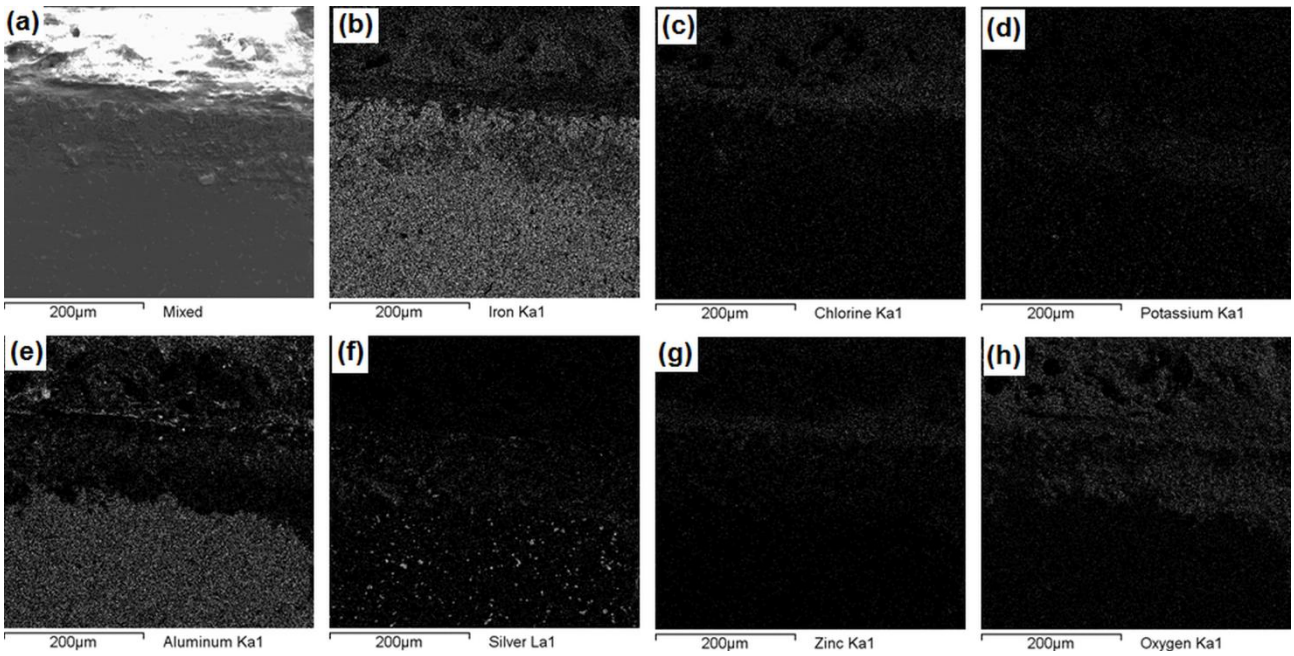

Figure 9. Photomicrographs of (a) Fe40Al2.5Ag corroded in the KCl+$ZnCl_2$ mixture at 450°C together with X-ray mappings of (b) Fe, (c) Al, (d) Ag, (e) Cl and (f) O.

In addition, according to Figures 9 b) and 9 h), there are some Fe and O present in top surface of alloy, indicating the presence of a layer composed by Fe_2O_3 or Fe_3O_4 which is in agreement with the wide region of stability of these iron oxides as predicted by the phase-stability diagram shown in Figure 11 a).

Corrosion morphology of Fe40Al2.5Ag ternary alloy together with the corresponding X-ray mappings of Fe, Al, Ag, Cl, K, Zn and O is shown in Figure 9.

Dealloying of Al is shown in top surface of sample; see Figure 9 e). This behavior is due to the fact that Al is the most reactive element of the ternary alloy system. Besides, the demetallification of Al was due to the diffusion of chlorine ions through cracks and porosity of the scale down to the matrix scale interface, where it reacted with the ternary alloy to form the volatile aluminum chloride, in accordance to the reaction 2 included in Table 2.

Since the liquid to gas phase transition of $AlCl_3$ occurs at approximately 178 °C [32, 33], the metal chloride diffused out of the scale, resulting in a lack of Al under the protective aluminum oxide layer.

Considering that the oxygen partial pressure at the matrix salt interface is low, iron from Fe40Al2.5Ag alloy is dissolved in the molten salt as a soluble iron chloride compound, in accordance to the reaction shown in Equation 1:

$$Fe+3Cl_{2\,(diss)} = 2FeCl_{3\,(diss)} \quad (1)$$

The dissolved iron (III) chloride compound diffuses outward to the salt/gas interface, where iron (III) oxide is precipitated again according to the reaction shown in Equation 2:

$$2FeCl_{3\,(diss.)} + 3/2\ O_2 = Fe_2O_3 + 3Cl_2. \quad (2)$$

The presence and location of Fe_2O_3 is corroborated by observing the x-ray mappings shown in Figures 9 h) y 9 b). These illustrations exhibit Fe and O elements located inside of corroded film of Fe40Al2.5Ag and above just within the corrosion products region. Since the iron oxide scale formed in this manner is poorly adherent and porous, it won't provide an efficient protection. Previous investigations have also reported iron oxide formation of ferrous alloys exposed to molten salts. Spiegel [34] studied the hot corrosion behavior of low-alloy steels exposed to $ZnCl_2$ at 500 and 600 °C under (He-5%O_2, $H_2O<10^{-4}$bar) gas mixture. The authors discovered that the low-alloy steel exposed to molten $ZnCl_2$ resulted in a formation of oxide layer composed mainly by Fe_3O_4 and a $ZnFe_2O_4$ spinel. Thus, the presence of Zn detected in the chemical mapping illustrated in Figure 9 g), could be attributed to a zinc oxide or zinc ferric-oxide spinel formation.

Based on the test results displayed in Figures 8 and 9, the corrosion of FeAl based alloys by the chloride melt were assumed to be mainly due to the presence of salt mixture in liquid phase and the fluxing (dissolving) of the protective oxide layer.

Pure silver precipitates are displayed uniformly distributed mainly in Fe-Al matrix and bellow the zone where Al was depleted, see Figure 9 f). The same precipitation behavior of Ag is observed in micrographs of un-corroded alloys, exhibited in Figure 1 b). A reduction of silver concentration together with a decrement of its precipitate size, is observed in the region where Al content was depleted, this behavior could be related to the formation of silver chloride according to reaction 12 included in Table 2. The formation of AgCl is consistent with phase predictions included in thermodynamic stability diagram shown in Figure 11. In this illustration, can be observed that silver

chloride exists throughout the biggest interval of oxygen partial pressure (Po_2). Once silver chloride was formed, could have been dissolved in the molten salt mixture and after was diffused out to substrate/molten salt interface.

3.6 Phase-stability thermodynamic analysis.

Clearly, it is well known, that a determinate amount of molten salt together with alloy elements and addition elements, available to interact by chemical reactions (with rich-oxygen environments) in open chemical systems, tend to form products in chemical equilibrium. This constitutes basically, the way to obtain the equilibrium constant of each chemical reaction in order to study the thermodynamic stability of phases along with their respective phase transitions involved in this kind of reaction systems. As a result of the oxidation reactions, we keep in mind that the thermodynamic studies may assist to improve the understanding of the corrosion mechanism in environments containing chlorine or oxygen [25, 26]. Indeed, there is a great probability that the thermodynamic of the oxidation reactions are related with the phase-change of materials.

For the chemical system composed by the triad of elements (M-Cl-O) (where M corresponds to Fe, Al or Ag taken at unit activity), it has been elaborated a thermodynamic stability diagram for a temperature of 450 °C. According to the typical temperatures that have been measured in waste incinerator systems, a temperature minor to 450°C was not very suited.

The thermodynamic analysis was performed in order to predict and also to confirm the corrosion products revealed in the experimental chemical mappings. The chemical composition distributed as atomic species can be observed in Figures 8 and 9. The chemical analysis for metallic elements (Fe, Al, Ag) and chlorine or oxygen elements, indirectly reveals the principal chemical products and metallurgical phases. Additionally, the phase stability diagrams were computed from equilibrium constants of chemical reactions. This thermodynamic study justifies the need of prove the formation of metallic oxides as a result of alloy degradation in an oxidation environment.

The thermodynamic equilibrium constants can be used, for instance, to know if the chemical system will react nearly to completion. To understand the significance of establishing an equilibrium constant for an oxidation reaction, the Table 2 shows the equilibrium constant of possible chemical reactions that should occur in the experimental reaction system designed in present work. The equilibrium constants were calculated assuming an ideal behavior for the gas phase. The chemical transformations of actual oxidation reactions have a characteristic condition of equilibrium to react to form products. Associated with the equilibrium state, the Figures 11 a) and 11 b) show the thermodynamic stability diagrams for Fe-Al-Ag-Cl-O and Ag-Cl-O at 450 °C respectively.

Depending upon the magnitude of the equilibrium constants and the amount of concentration of reactants and products the oxidation reaction will occur until equilibrium condition is attained. The chemical analyses performed by the scanning electron microscope revealed the formation of metallic oxides together with metallic chlorides in corroded specimens; it is worth noting, that these oxide and chloride compounds are in agreement with the predicted ones. The metal oxides predicted by the thermodynamic stability diagrams are expressed in terms of elemental mapping throughout the Figures

8 and 9. A complete agreement of chemical oxides predicted and observed, is considered a potential chemical system.

Thermodynamic computations show that $ZnCl_2$ contained in the chloride melt will be oxidized at 450 °C at the standar pressure of test (1 atm) and low partial pressure of chlorine P_{cl} (below 0.001 atm). Oxidation of $ZnCl_2$ can be represented by reaction included in Equation 3, as follows:

$$ZnCl_2 + 0.5O_2 = ZnO + Cl_2 \quad (3)$$

Table 1. Equilibrium constants for chemical reactions for the system K-Zn-Cl-O at 450°C.

#	Reaccion	Log K
1	$2\ K_2O(s) + 2\ Cl_2 = 4\ KCl(s) + O_2$	68.4026
2	$2\ K(l) + Cl_2 = 2\ KCl(s)$	53.0622
3	$2\ Zn(l) + O_2 = 2\ ZnO\ (l)$	39.831
4	$4\ K(l) + O_2 = 2\ K_2O(s)$	37.7219
5	$K_2O_2(s) + Cl_2 = 2\ KCl(s) + O_2$	28.9528
6	$2\ KO_2(s) + Cl_2 = 2\ KCl(s) + 2\ O_2$	27.0377
7	$Zn(l) + Cl_2 = ZnCl_2\ (s)$	22.2035
8	$2\ K_2O(s) + O_2 = 2\ K_2O_2(s)$	10.497
9	$2\ ZnO\ (s) + 2\ Cl_2 = 2\ ZnCl_2\ (s) + O_2$	4.5761
10	$K_2O_2(s) + O_2 = 2\ KO_2(s)$	1.9151

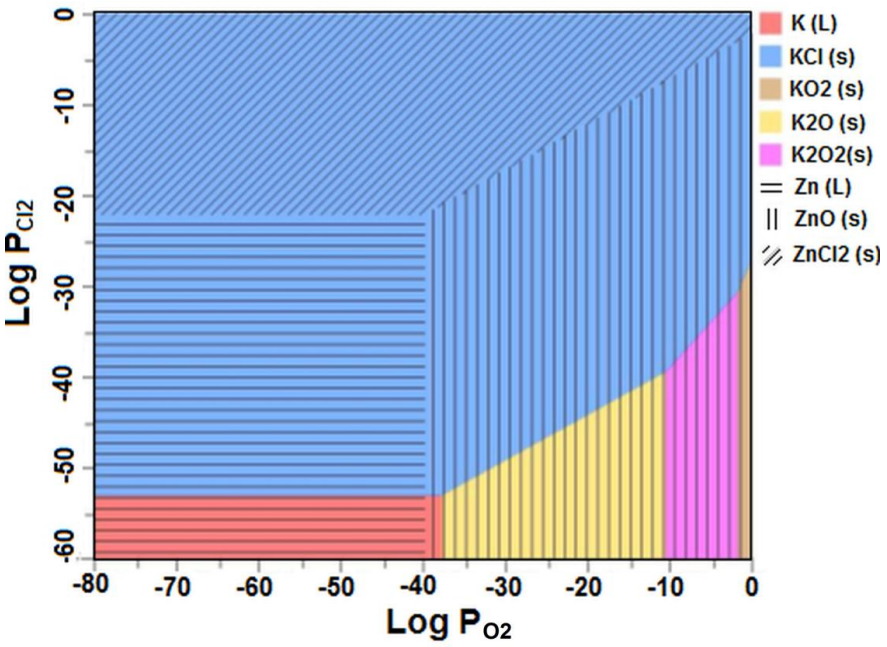

Figure 10. Thermodynamic stability diagram for K-Zn-Cl-O at 450 °C.

The presence of zinc oxide formed by equation 3 can be corroborated by observing the chemical mappings shown in Figures 9 g) and h). In these photomicrographs, Zn and O are present from the corroded zone of alloy to the substrate/chloride melt interface. Besides, the presence of ZnO

can be corroborated by the wide region in which this oxide exists in the phase stability diagram shown in Figure 10. The reaction of oxidation of $ZnCl_2$ will produce a chloride melt enriched with KCl which may react with the Fe oxide present on FeAl-base alloy as indicated in reaction represented by Equation 4.

$$4KCl\ (l) + 2Fe_2O_3(s) + O_2(g) = 2K_2Fe_2O_4(s) + 2Cl_2(g) \qquad (4)$$

The formation of $K_2Fe_2O_4$ compound can be justified by observing the chemical mappings included in Figures 9 b), d) and h) where the elements Fe, K and O can be observed from corroded zone of sample to oxide/chloride melt interface. Spiegel [34], reported also the formation of $K_2Fe_2O_4$ compound from the reaction of potassium chloride with hematite in a study of the hot corrosion behavior of steels and nickel-based alloys exposed to a $ZnCl_2$- KCl mixture at 300–600 °C. The formation of $FeCl_2$ and $FeCl_3$ can be inferred from the existence of Fe and Cl as revealed in the chemical mappings displayed in Figures 8 and 9. The existence of iron chlorides can be confirmed by looking at the phase stability diagram displayed in Figure 11, where is observed the wide interval of P_{o2} in which these chlorides are stable in an interval delimited by normal and moderate values of P_{Cl2} .When iron chloride diffuses outward to zones where the oxygen partial pressure predominates, the iron chloride compound may be transformed to hematite according to reaction 9 included in Table. Then, Cl_2 may diffuse back again to substrate/salt melt interface serving as new chlorine source for a subsequent iron chloride formation. In this manner, a catalytic cycle is achieved since no chlorine will be consumed.

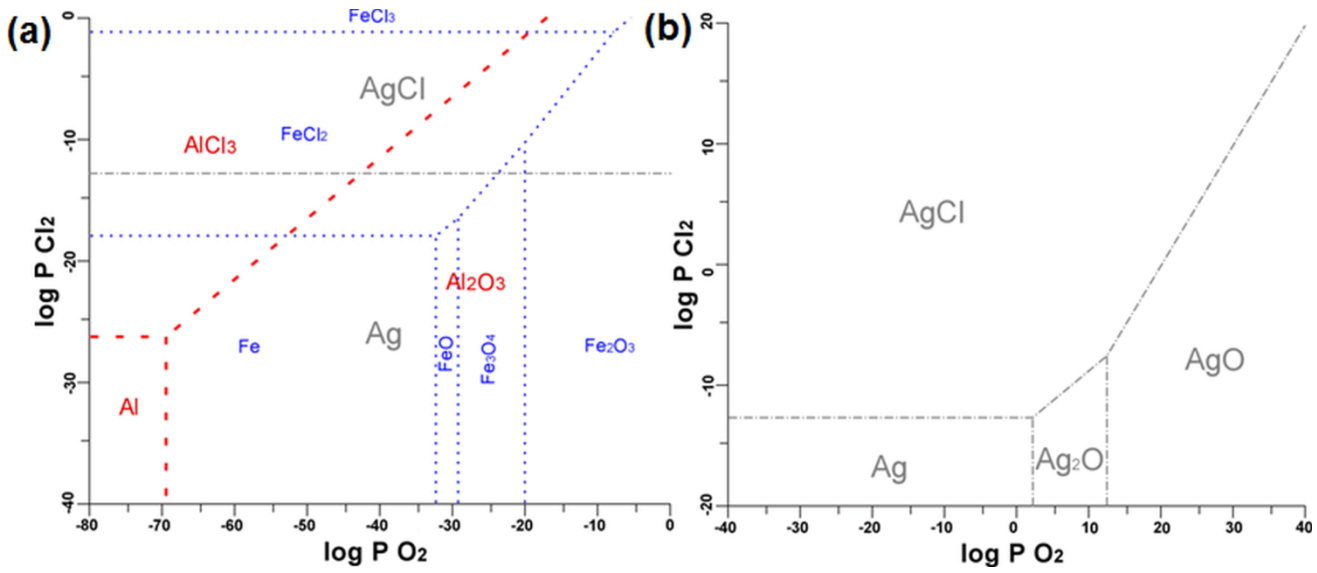

Figure 11. Thermodynamic stability diagrams for Fe-Al-Ag-Cl-O at 450 °C, at a) low and b) high oxygen partial pressures (P_{o2}).

Similarly, the Cl_2 produced by Equation 4 dissolves into the molten salt and acts as an oxidant for Fe in the FeAl-based materials; at the alloy/salt melt interface, the chlorine partial pressure P_{Cl2} leads to the formation of iron chlorides (reaction 10 included in Table 2 and Equation 1) because the P_{O2} is very low at the interior of the chloride melt. Ruh et al. [35] studied the kinetics of hot corrosion

of Fe, Cr and Ni covered by a molten KCl-$ZnCl_2$ mixture at 320 °C in an atmosphere consisting of argon and oxygen. The authors also reported the formation of $FeCl_2$ according to reaction 10 included in table 2. Similarly, Li et al. [36] corroded pure Fe, Cr, Ni and Fe-based alloys with a 55$ZnCl_2$-45KCl (mol %) mixture at 400-450 °C in pure O_2. In the same way, the authors stated the formation of $FeCl_3$ according to Equation 1.

Table 2. Equilibrium constants for chemical reactions for the system Fe-Al-Ag-Cl-O at 450°C.

#	Reaction	Log K
1	4 Al(s) + 3 O_2 = 2 Al_2O_3(s)	209.297
2	2 Al(s) + 3 Cl_2 = 2 $AlCl_3$(l)	79.0157
3	4 $AlCl_3$(l) + 3 O_2 = 2 Al_2O_3(s) + 6 Cl_2	51.2659
4	2 Fe(s) + O_2 = 2 FeO(s)	32.3568
5	6 FeO(s) + O_2 = 2 Fe_3O_4(s)	29.3604
6	2 Ag_2O (s) + 2 Cl_2 ⇔ 4 AgCl (s) + 1 O_2	27.6350
7	4 Fe_3O_4(s) + O_2 = 6 Fe_2O_3(s)	20.0696
8	2 AgO (s) + 1 Cl_2 ⇔ 2 AgCl (s) + 1 O_2	20.0453
9	4 $FeCl_2$(s) + 3 O_2 =2 Fe_2O_3(s) + 4 Cl_2	18.8497
10	Fe(s) + Cl_2 = $FeCl_2$(s)	18.0318
11	4 $FeCl_3$(l) + 3 O_2 =2 Fe_2O_3(s) + 6 Cl_2	16.5278
12	2 Ag(s) + 1 Cl_2 ⇔ 2 AgCl (s)	12.7159
13	3 $FeCl_2$(s) + 2 O_2 = Fe_3O_4(s) + 3 Cl_2	9.1198
14	2 FeO(s) + 2 Cl_2 = 2 $FeCl_2$(s) + O_2	3.7069
15	2 $FeCl_2$(s) + Cl_2 = 2 $FeCl_3$(l)	1.161
16	4 Ag(s) + 1 O_2 ⇔ 2 Ag_2O (s)	-2.2033
17	2 Ag_2O (s) + 1 O_2 ⇔ 4 AgO (s)	-12.4555

4. CONCLUSIONS

A study of the effect of adding 2.5 at. % Ag on the corrosion behavior of Fe40Al in molten salt mixture KCl-$ZnCl_2$ (1:1M) at 450°C was performed by means of electrochemical techniques. Polarization curves showed that by adding Ag, the corrosion rate of alloy was increased and the corrosion potential of Fe-Al-Ag alloy resulted nobler.

Binary Fe40Al alloy studied in this work exhibited a greater resistance to corrosion than Ni alloys (Ni-20Cr wt.%) and 304 SS steel under the same experimental test conditions of corrosion. Fe40Al2.5Ag alloy exhibited a more noble corrosion potential but a bigger corrosion rate than the 304 SS specimen corroded under the same experimental conditions. FeAlAg alloy presented a bigger corrosion rate than Ni20Cr wt% coating deposited on 304 SS. Nowadays, these last two materials are considered as candidate alloys for high-temperature processes such as combustion and high-power operations.

The mean values of polarization resistance (R_p) of FeAlAg alloy resulted minor that those of Fe40Al alloy. This behavior is associated to the higher corrosion rate of FeAlAg alloy as compared with binary alloy.

EIS data indicated that the corrosion rate was controlled by the formation of an external corrosion products film, which was dissolved by the Cl-containing molten salt.

In general terms addition to Ag to Fe40Al alloy induced a deleterious effect on its corrosion resistance. This behavior is due to the galvanic corrosion effects induced by the formation of Ag precipitates, since these precipitates possess a nobler corrosion potential with respect to the Fe-Al alloy components, promoting in this way a localized corrosion attack.

We conclude that in particular Fe40Al alloy show great promise for applications involving high-temperature processes like combustion and high-power operations with its high corrosion resistance, which may provide a longer and more stable product life for incinerator heat exchanger linings.

ACKNOWLEDGEMENT
The authors express their gratitude to CONACyT for the financial support granted for the development of this research.

References

1. M. J. Quina, J. C. Bordado and R. M. Quinta-Ferreira, *J. Hazard. Mater*., 179 (2010) 382.
2. E. Autret, F. Berthier, A. Luszezanec and F. Nicolas, *J. Hazard. Mater*., B139 (2007) 569.
3. T.S. Sidhu, S. Prakash and R.D. Agarwal, *Corros. Sci*., 90 (2006) 41.
4. S. Lee, N.J. Themelis and M.J. Castaldi, *J. Therm. Spray Technol*., 16 (2007) 104.
5. H. Zwaher, 11th North America WTE conference, Florida, Tampa, 2003.
6. C.T. Sims, N.S. Stoloff, W.C. Hagel, *Superalloys II*, John Wiley & Sons, New York, NY (1987).
7. Y. Kawahara, *Corros. Sci.*, 44 (2002) 223.
8. R.A. Rapp and Y.S. Zhang, *JOM*, 46 (1994) 47.
9. L. Nylöf and E. Häggblom, CORROSION 97, Paper No. 154 (1997).
10. V.K. Sikka, D. Wilkening, J. Liebetrau and B. Mackey, *Mater. Sci. Eng*., A258 (1998) 229.
11. J.H. DeVan and P.F. Tortorelli, *Corros. Sci.*, 35 (1993) 1065.
12. N.S. Stoloff, C.T. Liu and S.C. Deevi, *Intermetallics*, 8 (2000) 1313.
13. Y.S. Li, M. Spiegel and S. Shimada, *Mater. Chem. Phys*., 93 (2005) 217.
14. Y.S. Li and M. Spiegel, *Corros. Sci.*, 46 (2004) 2009.
15. E. M. Zahrani and A.M. Alfantazi, *Corros. Sci*. 65 (2012) 340.
16. E. Otero, A. Pardo, F. J. Perez, M. V. Utrilla, and T. Levi, *Oxidation of Metals*, 49 5-6 (1998) 467.
17. C.L. Zeng and J. Li, *Electrochimica Acta*, 50 28 (2005) 5533.
18. C. L. Zeng, W. Wang, and W. T. Wu, *Corrosion Science*, 43 4 (2001) 787–801.
19. T.B. Massalski, *Binary alloy phase diagrams*, 1 (1986) 112.
20. C. G. McKamey and N. S. Stoloff, *Physical Metallurgy and Processing of Intermetallic Compounds*, Pergamon, Oxford (1967).
21. F. Lihl and H. Ebel, *W. B. Pearson, a Handbook of lattice spacings and structures of metals and alloys*, Pergamon Press, New York (1967).
22. T.B. Massalski, *Binary Alloy Phase Diagrams*, 1 (1990) 35.
23. T.B. Massalski, *Binary Alloy Phase Diagrams*, 1 (1990) 8.
24. G. Salinas, J. G. Gonzalez-Rodriguez, J. Porcayo-Calderon, V. M. Salinas-Bravo, and M. A. Espinoza-Medina, *International Journal of Corrosion*, vol. 2012, Article ID 185842, 7 pages, 2012. doi:10.1155/2012/185842

25. J. Porcayo-Calderon, O. Sotelo-Mazón, V.M. Salinas-Bravo, C.D. Arrieta-Gonzalez, J.J. Ramos-Hernandez and C. Cuevas-Arteaga, *Int. J. Electrochem. Sci*., 7 (2012) 1134.
26. R. A. Rodríguez-Diaz, J. Uruchurtu-chavarín, J. Porcayo-Calderon, J. M. López-Oglesby, M. E. Mendoza, J. J. Ramos-Hernández, S. Valdez and A. Bedolla, *Int. J. Electrochem. Sci*., 8 (2013) 7257.
27. R. A. Cottis and S. Turgoose, *Electrochemical Impedance and noise; Corrosion Testing Made Easy Series*, NACE International (1999).
28. R. H. Jones and R. E. Ricker, *Environmental Effects on Advanced Materials*, The Minerals, Metals and Materials Society, Pennsylvania (1991).
29. P. F. Tortorelli and K. Natesan, *Mater. Sci. Eng*., A258 (1998) 115-125.
30. F. R. Duke and R. A. Fleming, *J. Electrochem. Soc*., 253 (1957) 104.
31. I. Kim and W. D. Cho, Mater. Sci. Eng. A 264 (1999) 269.
32. M. J. O'Neil, *The Merck Index: An Encyclopedia of Chemicals, Drugs, and Biologicals*, 14th Edition, Merck, New Jersey (2006).
33. A. F. Wells, *Structural Inorganic Chemistry*, Oxford University Press, Oxford, UK (1984).
34. M. Spiegel, *Mater. Corros*., 50 (1999) 373.
35. A. Ruh and M. Spiegel, *Corros. Sci*., 48 (2006) 679.
36. Y. S. Li, Y. Niu and W. T. Wu, *Mater. Sci. Eng*. A 345 (2003) 64.